Functionalized *de Novo* Designed Proteins: Mechanism of Proton Coupling to Oxidation/Reduction in Heme Protein Maquettes†

Julia M. Shifman,‡ Christopher C. Moser,‡ William A. Kalsbeck,§ David F. Bocian,§ and P. Leslie Dutton*,‡

Johnson Research Foundation, Department of Biochemistry and Biophysics, University of Pennsylvania, Philadelphia, Pennsylvania 19104, and Department of Chemistry, University of California, Riverside, Riverside, California 92521

Received July 13, 1998; Revised Manuscript Received September 29, 1998

ABSTRACT: Proton exchange with aqueous media coupled to heme oxidation/reduction is commonly seen but not understood in natural cytochromes. Our synthetic tetrahelix bundle heme protein maquettes successfully reproduce natural proton coupling to heme oxidation/reduction. Potentiometry reveals major p*K* shifts from 4.2 to 7.0 and from 9.4 to 10.3 in the maquette-associated acid/base group(s) upon heme reduction. Consequently, a 210 mV decrease in the heme redox potential is observed between the two extremes of pH. Potentiometry with resonance Raman and FTIR spectroscopy performed over a wide pH range strongly implicates glutamate side chains as the source of proton coupling below pH 8.0, whereas lysine side chains are suggested above pH 8.0. Remarkably, the p*K* values of several glutamates in the maquette are elevated from their solution value (4.4) to values as high as 7.0. It is suggested that these glutamates are recruited into the interior of the bundle as part of a structural rearrangement that occurs upon heme binding. Glutamate to glutamine variants of the prototype protein demonstrate that removal of the glutamate closest to the heme diminishes but does not abolish proton exchange. It is necessary to remove additional glutamates before pH-independent heme oxidation/reduction profiles are achieved. The mechanism of redox-linked proton coupling appears to be rooted in distributed partial charge compensation, the magnitude of which is governed by the dielectric distance between the ferric heme and acid/base side chains. A similar mechanism is likely to exist in native redox proteins which undergo charge change upon cofactor oxidation/reduction.

Oxidation/reduction of redox cofactors in proteins is frequently coupled to proton exchange with the external aqueous medium. Proton binding/release provides a ready means for the protein to respond to profound changes in the electrostatic potential caused by the redox reaction (*1*−*3*). Two cases of proton coupling to oxidation/reduction are observed in nature. For quinones and flavins, the negative charge introduced upon reduction can be fully compensated by proton binding to the ring substituents where the negative charge resides. The other class of redox cofactors, including the protein-ligated iron−sulfur clusters and hemes, cannot bind protons to completely cancel the charge changes occurring between the ferric and ferrous iron states. In these cases, charge compensation through proton exchange is assumed to involve the protein medium that supports the redox center, occasionally being described as a redox-Bohr effect (*4*−*6*).

Proton coupling to cofactor oxidation/reduction requires that an acid/base group shifts its p*K* value depending on the oxidation state of a redox cofactor (*7*−*9*). Oxidizing the cofactor increases its positive charge, which thereby reduces the proton affinity of an acid/base group. Thus, the p*K* of an acid/base group is generally lower when the cofactor is in the oxidized state. It follows that the redox midpoint potential of the cofactor will in turn depend on the protonation state of the acid/base group. Coupling to protonation of a single acid/base group will cause the heme redox potential to decrease with a slope of about −60 mV/pH unit in the pH range between the p*K* values in the oxidized (pK_{ox}) and in the reduced state (pK_{red}) and will be independent of pH outside this range.

The most dramatic p*K* shifts for redox centers occur when the proton binds directly to the reduced redox center; for example, the one-electron reduction of quinone to semiquinone shifts the p*K* from about −7 to +5 (*10*, *11*). Despite the fact that such a direct mechanism is not possible for iron−sulfur clusters and hemes, redox-linked p*K* shifts have been implicated in proteins containing those centers. Bioenergetically significant redox-linked proton exchange is evident in the pH-dependent redox potentials of the iron−sulfur clusters $N1_A$ and N2 of NADH−ubiquinone oxidoreductase (Complex I) (*12*−*15*), the b_L and b_H hemes of ubiquinone−cytochrome *c* oxidoreductase (Complex III) (*9*, *16*, *17*), and the *a* and a_3 hemes of cytochrome *c* oxidase (Complex IV) (*18*, *19*). While all these membrane complexes are either directly or indirectly involved in transmembrane proton pumping (*15*), it remains to be established if such pH-dependent properties of the described cofactors are essential

† This work was supported by U.S. Public Health Service Grants GM-48130 (P. L.D.) and GM-36243 (D.F.B.).

* To whom correspondence should be addressed. Phone: (215)-898-8699. E-mail: dutton@mail.med.upenn.edu. Fax: (215)-573-2235.

‡ University of Pennsylvania.

§ University of California, Riverside.

10.1021/bi9816857 CCC: $15.00
Published on Web 11/05/1998

for the vectorial proton movement. It is pertinent to note that some *c*-type cytochromes including cytochromes c_2, c'', c_{551}, and c_{554} also display pH-dependent redox potentials (*20*−*23*), although such dependence cannot easily be assigned to a particular biological function. Thus, while proton exchange mediated by protein structure could be a means to establish in vivo cofactor redox potentials, or to effect redox-driven proton pumping in energy conversion, it is possible that in many cases proton coupling may be merely incidental. Furthermore, relatively little is known about the actual mechanisms that are available to couple protons to cofactor oxidation/reduction.

Identification of the proton binding/release site(s) coupled to cofactor redox reactions remains a major challenge. The difficulties are rooted in the complexity of natural redox proteins which are only stable or soluble within a narrow pH range. There are only a few examples where the acid/base groups involved in proton coupling have been identified directly. For example, NMR[1] studies have shown that heme propionates can shift their p*K* values by about 1 pH unit in some *c*-type cytochromes (*21*, *22*, *24*). In some cases, changes in heme axial ligation have been observed that are plausibly associated with up to 2−3 pH unit redox-linked p*K* changes (*23*, *25*−*30*). Deprotonation of a heme ligating histidine (*31*, *32*) as well as proton binding/release on protein side chains (*24*) has also been suggested to cause pH dependencies of heme redox potentials. Site-directed mutagenesis has usually produced disappointingly small effects on proton-coupled redox reactions [see, for example, (*33*)]. An exception is provided by a model study on myoglobin (*34*, *35*), in which replacement of Val 68 in the heme pocket with a Glu or Asp lowers the heme redox potential by about 200 mV and introduces conspicuous pH dependency of the redox potential, clearly signaling a proton-coupled redox reaction.

We believe that many of the difficulties in understanding the mechanism of proton-coupled oxidation/reduction of heme proteins can be circumvented by designing and synthesizing a family of simplified model proteins, maquettes of complicated natural counterparts. The design is based on a four-helix bundle structural motif present in many key electron-transfer proteins, but in particular ubiquinone−cytochrome *c* oxidoreductase. We modified the heptad repeat four-helix bundle design of DeGrado and co-workers (*36*) so it would successfully incorporate heme binding sites (*37*). These synthetic heme proteins display the significant advantages of small size, simple and easily changeable amino acid composition, high water solubility, and stability over a wide range of conditions while maintaining a low dielectric interior in contact with the heme (*37*, *38*). The hemes in the maquettes are axially bis-histidine-ligated and display nativelike redox, spectral, and EPR properties. In the present study, we have used heme protein maquettes to successfully engineer large redox-linked p*K* shifts. We have also identified the key features of the proton coupling mechanism and learned to control H^+/e^- coupling.

[1] Abbreviations: ^{t}Bu, *tert*-butyl; CD, circular dichroism; DME, dimethyl ester; DMSO, dimethyl sulfoxide; Fmoc, 9-fluorenylmethoxycarbonyl; FTIR, Fourier transform infrared; Gdn·HCl, guanidine hydrochloride; $\Delta G°$, difference in Gibbs free energy between denatured and folded protein; HPLC, high-performance liquid chromatography; NMR, nuclear magnetic resonance; RR, resonance Raman.

MATERIALS AND METHODS

Protein Design and Assembly. The tetra-α-helix bundle design was based on the heptad repeat strategy where the assembly of helices is predominantly driven by the hydrophobic effect (*36*, *39*, *40*). The bundle core is comprised mostly of hydrophobic leucines with phenylalanines and heme-ligating histidines. The exterior of the bundle is composed of polar lysines and glutamates that confer water solubility to the peptide and potentially provide electrostatic stabilization of the bundle assembly. The present work was based on an early prototype protein design called "H10A24" (*37*). The prototype tetra-α-helix bundle was built from a 31 amino acid peptide with the sequence:

Ac-CGGGELWKLH**H**EELLKKFEELLKLAEERLKKL-CONH$_2$

This peptide was dimerized through the N-terminal cysteine to form a disulfide-linked 62 amino acid peptide, αssα, which spontaneously assembles to form a homodimeric $(\alpha ss\alpha)_2$ tetra-α-helix bundle in the aqueous phase. Histidines at positions 10 and 10′ of each αssα subunit were designed to accommodate one heme binding site close to the loop region; hence, $(\alpha ss\alpha)_2$ is capable of binding two hemes. It has previously been established that the two αssα subunits of the $(\alpha ss\alpha)_2$ bundle assemble in the *syn*-topology, so that the loops are at the same end of the bundle and the hemes are adjacent (*37*, A. M. Grosset, unpublished results). Figure 1 shows a working model of the prototype bundle including the features that will be referred to throughout this work.

Protein Synthesis. The 31 amino acid peptide was synthesized by a solid-phase method on a continuous flow MilliGen Model 9050 synthesizer utilizing a Fmoc/^{t}Bu protection strategy. N-Terminal acetylation of the peptide was performed with a 1:1 mixture of acetic anhydride/pyridine for 20 min. The peptide was cleaved from the resin, and the protecting groups on amino acids were removed by exposure to a 90:8:2 mixture of trifluoroacetic acid/ethanedithiol/water for 2 h. Crude peptide was precipitated with cold ether and then purified by reversed-phase Rainin HPLC with aqueous/acetonitrile gradients containing 0.1% trifluoroacetic acid. The 31 amino acid peptide was dimerized by oxidizing the N-terminal cysteine in air-saturated 100 mM ammonium bicarbonate buffer (pH 9) for 4 h. The purity of the disulfide-linked 62 amino acid αssα peptide was characterized on an analytical Beckman System Gold HPLC system. The protein mass of the purified prototype αssα (and variants) was verified to be 7443 kDa (as expected) by electrospray mass spectroscopy. The material was lyophilized and stored at −20 °C until required.

Solution Molecular Weight Determination. Beckman System Gold HPLC was used for gel filtration chromatography equipped with a Supelco GFC-100 column (7.5 × 300 mm) equilibrated at a flow rate of 0.5 mL/min with either of the following buffers in the presence of 100 mM NaCl: 50 mM Tris/HCl, pH 8.5; 50 mM citric acid, pH 4; 50 mM 3-(cyclohexylamino)-1-propanesulfonic acid (CAPS), pH 10. Column calibration was performed with a low molecular weight gel filtration calibration kit (Pharmacia Biotech, Uppsala, Sweden). Unless otherwise stated, the prototype and variant peptides eluted with retention times consistent with a tetra-α-helix bundle aggregation state, with less than 10% of the material comprising higher oligomerization states.

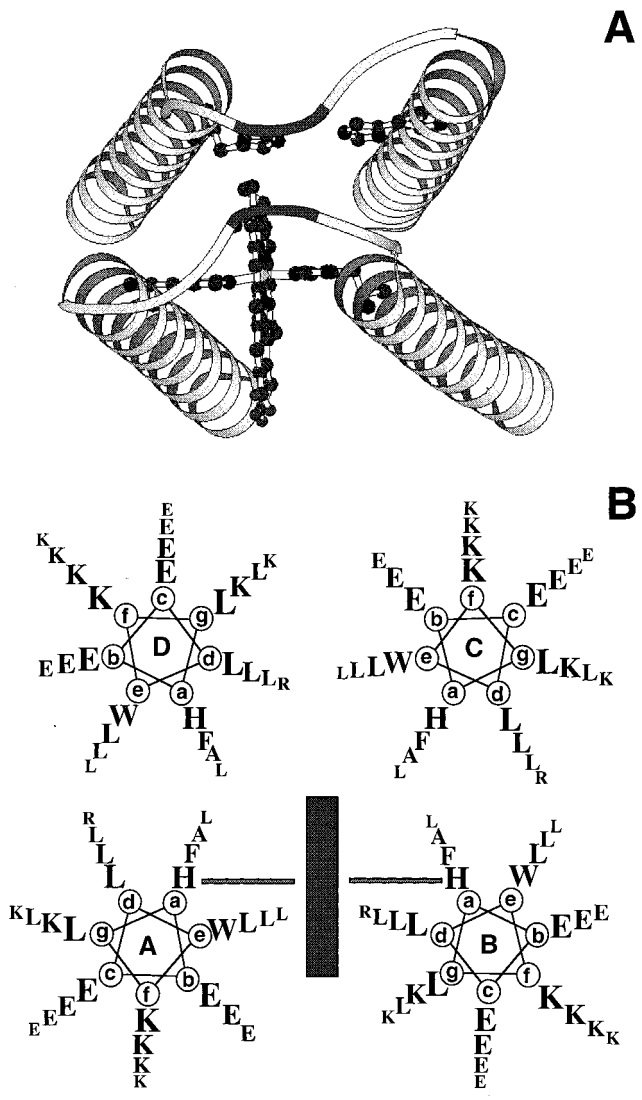

FIGURE 1: (A) A working model of the heme-(αssα)$_2$ maquette illustrating a single heme cofactor ligated to the bundle via two histidines and also showing two nonligating histidines in the adjacent αssα subunit. (B) A helical wheel representation of the bundle (residues 5−31 are shown, residues 1−4 of the loop region are excluded) displaying the heptad positions indicated by letters **a** through **g**.

A Beckman Optima XL-A analytical ultracentrifuge was used to perform equilibrium ultracentrifugation on the prototype maquette and its variants in the single heme bound form at both pH 8.5 and pH 4. The data were collected at three different peptide concentrations and two different centrifuge speeds (20 000 and 30 000 rpm). Partial specific volumes ($\bar{\nu}$) of the prototype and variants were calculated from the sequence as described in (*41*) and were used to fit the data to obtain the apparent molecular weight of the peptides.

UV−Visible Spectroscopy. The spectra were recorded on a Perkin-Elmer Lambda 2 spectrophotometer. The peptide concentration was determined optically by the absorbance of the Trp (position 7 on each α-helix), using $\epsilon_{280} = 5600$ M^{-1} cm^{-1}. Heme binding was monitored by loss of the absorption at 385 nm due to free hemin, and the concomitant appearance of a sharp Soret band at 412 nm, corresponding to heme bound to the protein via bis-histidine axial coordination.

Circular Dichroism. CD spectra were recorded on an Aviv Associates Model 60DS spectropolarimeter using a 2 mm quartz cuvette at 25 °C. The buffers used in the presence of 100 mM NaCl were 50 mM citric acid (pH 1−6), 50 mM Tris/HCl (pH 7−9), 50 mM boric acid (pH 9−10), and 50 mM 3-(cyclohexylamino)-1-propanesulfonic acid (CAPS) (pH 10−12). The helicity of the peptide was calculated from the absorbance at 222 nm (Θ_{222}) which was normalized to −32 000 deg cm^2 dmol. For the chemical denaturation experiments, dilutions of 8 M guanidine hydrochloride (Gdn·HCl; Pierce, Rockford, IL) and concentrated protein solution were performed to obtain a 10−20 μM protein, x M Gdn·HCl sample, where x varied from 0 to 7.8. The denaturation curves were fit to a dimer-folded to monomer-unfolded equilibrium model (*42*) to obtain $\Delta G°$ according to

$$\% \text{ folded} = 1 - \frac{\exp(-\Delta G^{\text{unf}}/RT)}{4P}\left[\left(1 + \frac{8P}{\exp(-\Delta G^{\text{unf}}/RT)}\right)^{1/2} - 1\right] \quad (1)$$

where $\Delta G^{\text{unf}} = \Delta G° - m$[Gdn·HCl], m is a parameter reflecting the cooperativity of the unfolding transition, and P is the molar concentration of total monomeric protein.

Heme Protein Preparation. The concentrated hemoprotein solution was prepared in advance by addition of 5 μL aliquots of a 10 mM solution of iron protoporphyrin IX (hemin; Porphyrin Products Inc., Logan, UT) in dimethyl sulfoxide (DMSO) to the stirred peptide in 10 mM Tris/HCl, 100 mM NaCl buffer, pH 8.5. Samples of the single-heme-bound protein, heme-(αssα)$_2$, were prepared by titration of only 0.8 heme equiv per four-helix bundle in order to keep the population of two-heme-bound species negligibly low. For FTIR spectroscopic measurements, all solutions were prepared in D_2O. The heme-bound peptide was concentrated in a low-speed Beckman J-21C centrifuge to reach a concentration of about 300 μM for redox experiments or 2−3 mM for FTIR experiments and stored at 4 °C. The dimethyl ester of iron protoporphyrin IX (DME-heme; Porphyrin Products Inc.) showed only partial binding to the peptide at a concentration of 10 μM. To avoid interference from the presence of free porphyrin in solution, only 0.2 equiv of DME-heme per (αssα)$_2$ of about 50−100 μM concentration was added.

Redox Titrations. Redox titrations were performed in combination with optical analysis, using the UV−visible spectrophotometer described above. The concentrated sample of hemoprotein prepared in advance was diluted to 5−10 μM into a buffer at a selected pH for each individual titration. The buffer solutions used were the same as those described above for the CD measurements. The redox titrations were performed using an in-house-designed glass redox cuvette with platinum measuring and calomel reference electrodes (Radiometer Analytical, Lyon, France) (*8*); the reported redox potentials are referenced to a standard hydrogen electrode. All redox titrations were performed anaerobically using <1 μL additions of freshly prepared sodium dithionite to adjust the solution potential to more negative values and potassium ferricyanide to more positive values. The following redox mediators were used to stabilize solution redox potential: 20 μM duroquinone, 10 μM pyocyanine, 10 μM 2-hydroxy-1,4-naphthoquinone, 10 μM anthraquinone-2-sulfonate, 2 μM

benzyl viologen, 1 μM phenylsafranine, and 1 μM indigocarmine.

Redox Titration Data Analysis. All of the tetra-α-helix bundles show a typical bis-histidine-ligated heme spectrum with a Soret maximum at 412 nm in the oxidized state. In the reduced state, the Soret band gains intensity, narrows, and shifts to 425 nm; the sharp α-band at 559 nm and β-band at 535 nm characteristic of bis-histidine-ligated heme are evident in the reduced state. Redox titrations were analyzed by monitoring the absorbance bands at 559 and 425 nm as the heme protein was reduced or oxidized. The data were analyzed with the Nernst equation using an *n*-value of 1.0 in the case of one heme incorporated into the bundle:

$$\% R = \frac{1}{10^{(E-E_m)/[(RT/nF)]}} \quad (2a)$$

or two *n*-values of 1.0 when two hemes were present:

$$\% R = \frac{0.5}{10^{(E-Em_1)/[(RT/nF)]}} + \frac{0.5}{10^{(E-Em_2)/[(RT/nF)]}} \quad (2b)$$

where % *R* is the fraction of reduced heme, *E* is the solution redox potential, *n* is the number of electrons participating in the redox reaction, and E_m is the redox midpoint potential.

The E_m vs pH curves were analyzed according to a thermodynamic cycle where the redox reaction was coupled to proton exchange. The heme oxidation/reduction when coupled to protonation of *i* independent acid/base groups is described according to

$$E_m = E_0 + \frac{RT}{nF} \ln \frac{([H^+] + K^r_1)([H^+] + K^r_2) \ldots ([H^+] + K^r_i)}{([H^+] + K^o_1)([H^+] + K^o_2) \ldots ([H^+] + K^o_i)} \quad (3)$$

where E_0 is the redox midpoint potential at low pH, when all acid/base groups are protonated, $[H^+]$ is the proton concentration, K^r_i is the association constant for proton binding to the *i*th acid/base group in the reduced state of the heme, and K^o_i is the association constant for proton binding to the *i*th acid/base group in the oxidized state of the heme.

Resonance Raman Spectroscopy. The resonance Raman (RR) spectra were acquired with a Spex 1877 triple spectrograph equipped with a holographically etched 2400 groove/mm grating in the final stage. The scattered light was collected at 90° to the incident laser beam by use of a camera lens (Canon 50 mm f/1.4). The excitation wavelengths, provided by the outputs of a Coherent Innova 200-K3 Kr ion laser, were 413.1 nm for the ferric and 415.4 nm for the ferrous heme protein samples, respectively. A 1152 × 298 pixel, front-illuminated, UV-enhanced, charge-coupled device (CCD) was used as the detector (Princeton Instruments, Princeton, NJ; LN/CCD equipped with a EEV 1152-UV chip). The laser powers were typically 3−5 mW. The frequencies were calibrated using the known frequencies of indene and CCl_4. The frequencies are accurate to ±1 cm^{-1} for strong and/or isolated bands. The slit widths were set to provide ∼2 cm^{-1} resolution. The sample concentrations were about 100 μM.

FTIR Experiments. A Bruker IFS 66 FTIR spectrometer (Bruker Inc., Brookline, MA) equipped with a Globar source, a KBr splitter, and a MCT detector was used for the IR measurements. pH titrations in combination with FTIR were performed in a closed flow-through system with the sample solution circulated by a peristaltic pump from the closed vial to the ZnSe total internal reflection cell. A custom-made pH electrode (Microelectrodes Inc., Bedford, NH) was placed in the closed vial with about 100 μL of sample to measure the pH of the solution. To avoid the interference of the strong water absorption signal with the absorption of glutamates in the bundle, all experiments were performed in D_2O, and the measured pH values were subsequently converted to pD by the addition of 0.4 unit. Small aliquots (<1 μL) of 1 M DCl or NaOD were added to the vial to adjust the pD. For measurements with the heme in the reduced state, the apparatus was modified to ensure anaerobic conditions and to monitor the redox potential of the solution. A flow-through, custom-made, redox electrode (Microelectrodes, Inc.) was inserted in the tubing. The heme protein sample in the vial was kept under argon flow. In addition, the flow system was placed in a plastic bag and maintained under argon at a slight positive pressure. Sodium dithionite was added to the sample to ensure reducing conditions. After each addition, the sample was left to mix for several minutes before the spectrum was taken. Each spectrum was derived from 128 interferograms acquired with 0.5 cm^{-1} resolution. Water vapor and HOD contaminations to the spectra were subtracted followed by convolution to give a final resolution of 2 cm^{-1}. Spectral manipulations and determinations of peak positions were carried out using OPUS software (Bruker Inc.). Protonation of the glutamates was analyzed by monitoring the amplitude of the 1566 cm^{-1} peak with changing pD. The p*K* values were derived from fitting the data to the Henderson−Hasselbalch equation.

RESULTS

Single-Heme Binding to the Prototype Maquette. Although the prototype heme protein maquette can accommodate two hemes, one in each αssα subunit, for simplicity the present work focuses on the single-heme-bound form, heme-$(\alpha ss\alpha)_2$, as illustrated in Figure 1A. Figure 2A shows a binding isotherm of a single heme to the prototype protein, which yields a K_d value of 12 nM at pH 8.5. Binding of a second heme (not shown) to produce heme$_2$-$(\alpha ss\alpha)_2$ occurs with a K_d value of 800 nM, some 70-fold weaker. Using the specified K_d values and 10 μM peptide concentration, we calculated the fraction of peptides with two hemes bound, heme$_2$-$(\alpha ss\alpha)_2$, to be only 5% of the single-heme-bound species, heme-$(\alpha ss\alpha)_2$, upon the addition of 0.8 heme equiv per four-helix bundle. Since further titration of heme will result in an increase of the heme$_2$-$(\alpha ss\alpha)_2$ population to nonnegligible values, all experiments on heme-$(\alpha ss\alpha)_2$ were performed with 0.8 heme equiv added, leaving 20% of the bundles electrochemically inactive.

Figure 2B shows the course of oxidation/reduction of the heme-$(\alpha ss\alpha)_2$. The data are well described by a single $n = 1$ Nernst curve, demonstrating a remarkable electrochemical homogeneity of the bis-histidine-ligated heme in heme-$(\alpha ss\alpha)_2$. The $E_{m8.5}$ value is −156 ± 7 mV, which is substantially elevated from the aqueous solution value of bis-imidazole heme ($E_{m8.5}$ value approximately −235 mV; J. M. Shifman, unpublished results) and is consistent with a significantly buried state of the heme in the protein. Figure 2B also shows the redox titration of heme$_2$-$(\alpha ss\alpha)_2$ which

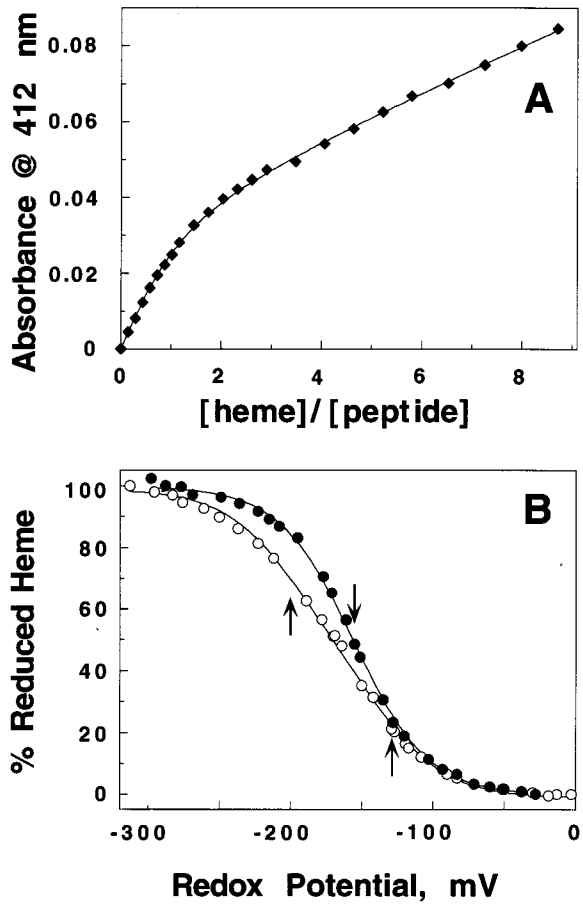

FIGURE 2: Heme binding and redox properties of the prototype maquette. (A) Heme binding isotherms for the $(\alpha ss\alpha)_2$ prototype maquette. Titration of hemin into a 36.5 nM tetra-α-helix bundle in a 10 cm path length cuvette at 25 °C. The absorbance at 412 nm is plotted against heme equivalents added to a tetra-α-helix bundle. The fit to a single heme binding event yields a K_d value of 12 nM. (B) Redox titration of heme-$(\alpha ss\alpha)_2$ (●) compared to heme$_2$-$(\alpha ss\alpha)_2$ (○) monitored by optical spectroscopy. The titrations were performed at pH 8.5 and 25 °C in 100 mM NaCl, 50 mM Tris/HCl buffer. The fraction of the reduced heme was determined by the change in absorbance at 559 nm (α-band maximum) relative to the base line absorbance (575 nm). The curves were fitted to eq 2a in the case of heme-$(\alpha ss\alpha)_2$ and eq 2b in the case of heme$_2$-$(\alpha ss\alpha)_2$ as described under Materials and Methods. Arrows indicate the fitted values of the redox potentials: -156 ± 7 mV for the heme-$(\alpha ss\alpha)_2$; -130 ± 15 mV and -200 ± 15 mV for the heme$_2$-$(\alpha ss\alpha)_2$.

exhibits two midpoint potentials split by 70 mV, in agreement with previous studies. This splitting is consistent with charge interaction between the adjacent ferric hemes across the interior of the bundle (*37*, *38*) and the *syn*-topology of the αssα subunits in the $(\alpha ss\alpha)_2$ tetrahelix bundle as shown in Figure 1A (A. M. Grosset, unpublished results).

Stability of the Prototype Maquette over a Wide pH Range. As required for a study of the proton coupling to the oxidation/reduction of heme-$(\alpha ss\alpha)_2$, we examined maquette stability over a wide range of pH conditions.

(A) α-*Helicity*. Figure 3A shows the helicity of the apo prototype maquette, $(\alpha ss\alpha)_2$, at various pH values monitored by CD. The data demonstrate that the α-helical content of the bundle remains unchanged from pH 1.0 to pH 12.0.

(B) Heme Affinity. Because the iron of the heme is coordinated to the bundle by two axial histidines and is subject to competition from protons and hydroxyls at the pH extremes, we also investigated the dissociation of the

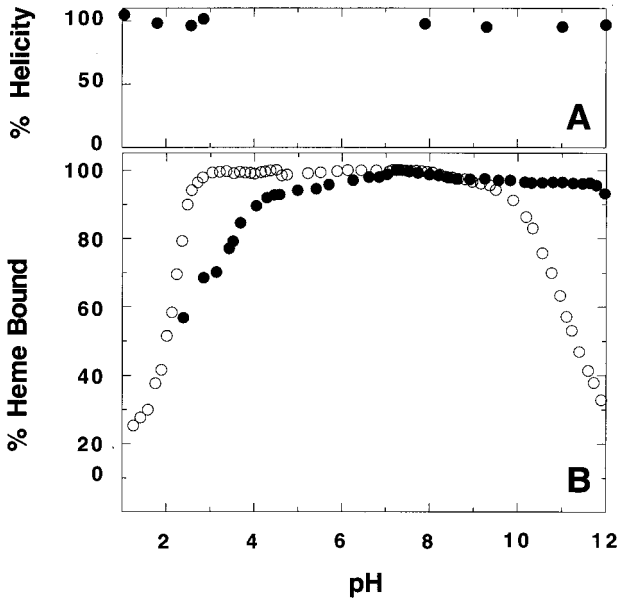

FIGURE 3: Stability of the prototype maquette as a function of pH. (A) Helical content of the apo prototype maquette as a function of pH normalized to the helicity at pH 8.5 as measured by the Θ_{222} at 25 °C. The buffers used in the presence of 100 mM NaCl were 50 mM citric acid (pH 1−6), 50 mM Tris/HCl (pH 7−9), 50 mM boric acid (pH 9−10), and 3-(cyclohexylamino)-1-propanesulfonic acid (CAPS) (pH 10−12). (B) Fraction of the heme bound to the prototype maquette as a function of pH in the oxidized state (○) and in the reduced state (●). The heme−protein sample was prepared in advance at pH 8 (where the heme affinity to the peptide is maximum), and then the pH was adjusted by additions of small aliquots of HCl or NaOH to lower or higher value. The sample was left for several minutes to equilibrate before the UV−visible spectrum was recorded. The data points were calculated from deconvolution of the visible spectra of the heme-$(\alpha ss\alpha)_2$ maquette into a bis-histidyl-bound heme spectra (Soret peak at 412 nm, $\epsilon = 110\,000$ M^{-1} cm^{-1} in the oxidized state which shifts to 425 nm, $\epsilon = 150\,000$ M^{-1} cm^{-1} in the reduced state) and free hemin spectra in aqueous solution. All data points were normalized to the pH 8 value.

heme from the bundle over the same pH range. The integrity of the heme−$(\alpha ss\alpha)_2$ complex was checked by following the amplitude of the narrow, prominent Soret band at 412 nm, characteristic of the protein-associated bis-histidine-ligated heme. Figure 3B shows that the heme remains fully bound to the peptide in both the ferrous and ferric forms over a pH range of 4−10. Outside this pH range, below pH 4 and above pH 12, the ferrous heme dissociates, while below pH 3 and above pH 10 the ferric heme dissociates. We attribute the heme dissociation in the high- and low-pH region to successful competition of hydroxyl ions and protons over ϵ-nitrogens of the heme-ligating histidines.

(C) Protein Assembly. The prototype heme-$(\alpha ss\alpha)_2$ maquette association state was investigated over a wide pH range by size-exclusion chromatography and equilibrium ultracentrifugation. Comparison of size-exclusion chromatography (pH 10.0 and 4.0) and equilibrium ultracentrifugation data (pH 8.5 and 4.0) revealed no substantial differences in the maquette molecular weight (not shown). Accordingly, the association state of the protein remains four-helix bundle throughout this pH range as originally determined at pH 8 (*37*).

Proton Coupling to Heme Oxidation/Reduction in the Heme-$(\alpha ss\alpha)_2$ Maquette. The pH dependency of the heme-

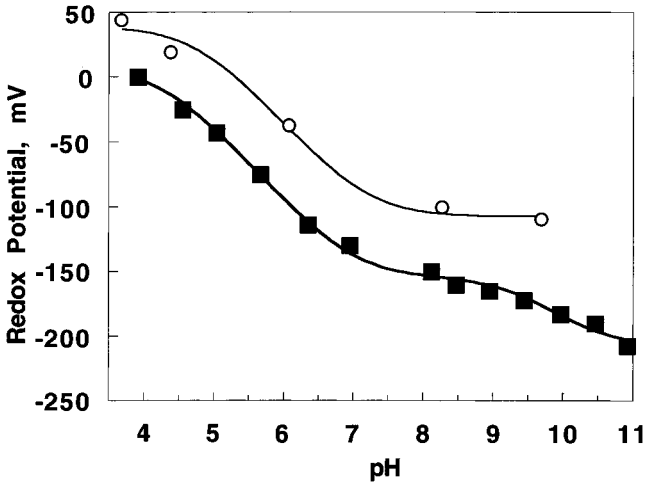

FIGURE 4: pH dependency of the redox midpoint potential of the prototype maquette incorporated with heme (■) [heme-$(\alpha ss\alpha)_2$] and DME-heme (○) [DME-heme-$(\alpha ss\alpha)_2$]. Each point represents an independent titration experiment as shown in Figure 2B. The buffers are the same as described in Figure 3A. The E_m/pH curves were fitted to eq 3 assuming independent protonations of two acid/base groups. The fitting procedure for heme-$(\alpha ss\alpha)_2$ yielded the following values: $pK^1_{ox} = 4.25$; $pK^1_{red} = 7.0$; $pK^2_{ox} = 9.4$; $pK^2_{red} = 10.3$.

$(\alpha ss\alpha)_2$ redox potential (E_m) is shown in Figure 4. The E_m/pH relationship displays two clear pH regions where the proton coupling to heme oxidation/reduction is evident. The major dependency of E_m on pH is manifested between pH 4 and 7, where the slope of the curve reaches the maximum theoretical value of approximately −60 mV/ pH unit. Between pH 7 and 9, the heme redox potential tends toward pH independence, but above 9 the pH dependency is apparent again. The E_m of the prototype maquette spans a total of 210 mV, representing a 4.8 kcal/mol change over a pH range from 4 to 11. The heme-$(\alpha ss\alpha)_2$ redox potential data can be fit using eq 3 to describe protonation of two different acid/base groups coupled to heme oxidation/reduction with $pK^1_{ox} = 4.25$; $pK^1_{red} = 7.0$; $pK^2_{ox} = 9.4$; $pK^2_{red} = 10.3$.

Identification of Acid/Base Groups Participating in Redox-Linked Proton Exchange. The small size and simple amino acid composition of the heme protein maquettes simplify the task for identification of the group(s) responsible for redox-linked proton binding/release (Figure 1B). There are only a few candidates available to perform proton coupling to heme redox reaction in the heme-$(\alpha ss\alpha)_2$ maquette. These are (a) the heme propionic acids with a solution p*K* of 4.9, (b) the histidines that coordinate the heme group, (c) the unligated histidines in the adjacent di-α-helix, and (d) the acid/base protein side chains in the heme vicinity which include glutamates (solution p*K* of 4.4) and lysines (solution p*K* of 10.0).

(A) Heme Propionic Acids. RR spectroscopy was used to investigate protonation changes in the peripheral propionic acid substituents of the heme macrocycle. The low-frequency region (225−450 cm^{-1}) of the Soret-excitation RR spectrum shows four distinct bands which have been previously characterized in natural heme proteins (*45*). Two of these modes contain contributions from motions of the propionic acid groups: (a) the heme skeletal vibration ν_9 (270 cm^{-1}), which results from a mixture of propionate and methyl group bending; and (b) the $\delta C_bC_1C_2$ (420 cm^{-1}) vibration, which results from an internal bending motion of the propionate chain. Inspection of the low-frequency region of the ferric heme maquette RR spectrum (not shown) reveals that the ν_9 mode experiences a clearly measurable upshift as the pH is lowered from neutral to acidic. The majority of the upshift occurs in the pH 6−4 range, where the band shifts from 268 to 272 cm^{-1}. The RR spectrum of the ferrous heme maquette (not shown) reveals similar shifts of the ν_9 band (268 to 273 cm^{-1}) between pH 7 and 5. The spectral alterations in the low-frequency RR spectra confirm that protonation of heme propionic acids takes place between pH 7 and 4. The RR data also suggest that heme protonation occurs approximately 1 pH unit higher in the reduced state relative to the oxidized state, although the relatively small RR spectral shifts of overlapping bands make precise quantification difficult without further experimentation.

To more directly assess the involvement of propionates in proton coupling to heme oxidation/reduction, we investigated the pH dependence of the redox characteristics of $(\alpha ss\alpha)_2$ reconstituted with DME-heme which is incapable of accepting protons on any of the substituents. Figure 4 shows the E_m/pH relationship of the DME-heme-$(\alpha ss\alpha)_2$. The E_m values of the DME-heme-$(\alpha ss\alpha)_2$ maquette are generally raised by 40−60 mV in comparison to those of the propionate containing heme-$(\alpha ss\alpha)_2$. The pH-dependent profile of the redox potential remains generally similar, strongly suggesting that propionates are not the primary source of proton coupling to heme oxidation/reduction in heme-$(\alpha ss\alpha)_2$, at least in the acidic pH range where RR shows propionate protonation/deprotonation. At present, there are less data in the alkaline range, allowing the possibility that propionates could be responsible for the pK_2. However, this seems highly unlikely since the solution p*K* of propionates would have to be elevated by at least 4 pH units in the presence of the oxidized heme, and by an extraordinary 5 pH units in the presence of the reduced heme.

(B) Heme-Ligating Histidines. The pH dependency of the heme redox potential in several natural cytochromes has been attributed to dissociation and substitution of one of the heme axial ligands (*23*, *25*−*30*) as well as to deprotonation of the nonligating nitrogens (Nδ-H) of the axial histidines (*31*, *32*). We used resonance Raman spectroscopy (RR), which is very sensitive to alterations in heme axial ligation, to investigate the possibility of such changes in the prototype maquette. At neutral pH, the heme-$(\alpha ss\alpha)_2$ maquette has been shown to exhibit a RR spectrum very similar to that of a bis-imidazole-ligated low-spin heme in solution (*38*). Figure 5 shows that between pH 9.5 and pH 2.9 neither the ferric nor the ferrous forms of heme-$(\alpha ss\alpha)_2$ display any detectable changes in the high-frequency Soret-excitation RR spectrum. Loss of one of the histidine ligands would have resulted in 10−20 cm^{-1} downshifts of the ν_{10} (1640 cm^{-1}), ν_2 (1580 cm^{-1}), and ν_3 (1507 cm^{-1}) bands of the ferric protein, and analogous changes would have been evident for the ferrous form. A change in heme ligand that retains the low-spin state of iron would be expected to yield smaller but still visible changes (3−5 cm^{-1}). The absence of alterations in the high-frequency RR and in UV−visible spectra of the heme-$(\alpha ss\alpha)_2$ maquette indicates that the heme macrocycle experiences no significant structural perturbations throughout the studied pH range (pH 2.9−9.5). In particular, the integrity of the bis-histidine axial ligation is preserved in

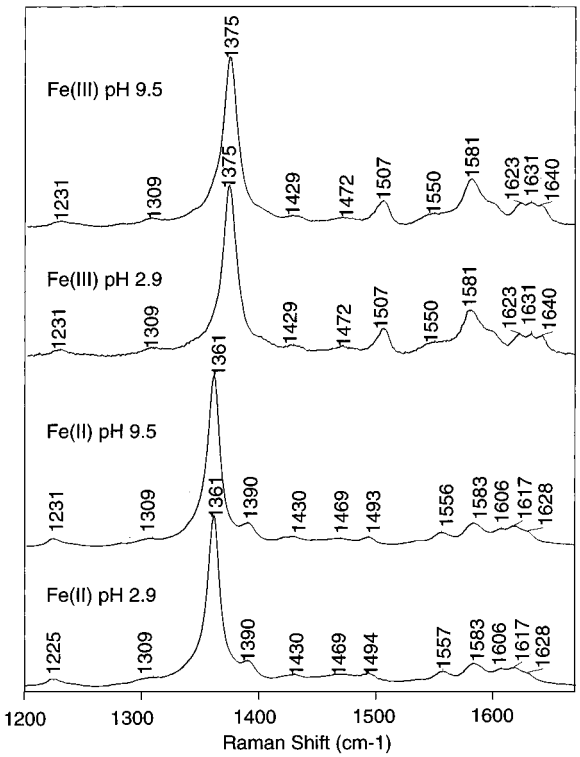

FIGURE 5: Resonance Raman spectra of the heme-$(\alpha ss\alpha)_2$. The high-frequency Soret-excitation RR spectra of the heme-$(\alpha ss\alpha)_2$ maquette in the ferric (λ_{ex} = 413.1 nm) and ferrous (λ_{ex} = 415.4 nm) states at high (pH 9.5) and low (pH 2.9) pH values. The protein samples of ~100 μM concentrations were prepared in the appropriate buffers as described in Figure 3.

the prototype maquette throughout the pH range studied.

In previous studies on bis-imidazole heme complexes (*43*) and on microperoxidase-8 (*44*) performed in the presence of a cationic detergent (CTABr), deprotonation of the heme axial ligands was observed with heme oxidation-state-dependent p*K* values above pH 9.0. Deprotonation of the imidazole/histidine axial ligand is indicated by a 5−7 nm red shift in the Soret absorption band as well as substantial changes in both the high- and low-frequency regions of the RR spectrum. The absence of similar alterations in the spectra of the prototype heme-$(\alpha ss\alpha)_2$ maquette argues that no deprotonation events on the Nδ-H of the heme axial ligands occur over the pH range studied.

(C) Histidines in the Adjacent **α*ss*α** *Subunit.* While ligation of the heme is not interrupted by protonation/deprotonation of the histidine ligands in heme-$(\alpha ss\alpha)_2$, two free histidines are present in the adjacent $\alpha ss\alpha$ subunit that could be close enough to the heme cofactor to become a potential source of proton coupling to heme oxidation/reduction. To test the possible involvement of these histidines in the redox-linked proton exchange, we examined the pH dependency of the maquette redox potential with two hemes bound, thereby removing any unligating histidines. Figure 6 shows that each heme in heme$_2$-$(\alpha ss\alpha)_2$ displays a pH-dependent profile generally similar to that of a single heme, thus ruling out the possibility that the histidines on the adjacent $\alpha ss\alpha$ subunit participate in proton coupling. A closer examination of the E_m/pH profile of the heme$_2$-$(\alpha ss\alpha)_2$ reveals that the pK value of the first reduced heme (pK_{red}) in heme$_2$-$(\alpha ss\alpha)_2$ is slightly lower compared to that of the second heme. The redox potential splitting between the two

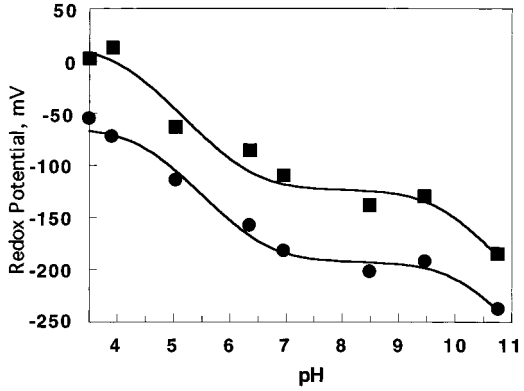

FIGURE 6: pH dependency of the redox potential of heme$_2$-$(\alpha ss\alpha)_2$. Each point represents an individual titration as shown in Figure 2B. The higher potential heme is represented by ■; the lower potential heme by ●.

cofactors in heme-$(\alpha ss\alpha)_2$ is evident across the entire pH range, diminishing slightly (by 20 mV) in the pH-dependent region (between pH 4 and 7), consistent with a lowered pK of the first heme reduced. These experimental findings, together with the results obtained with DME-heme, strongly suggest that the predominant source of the proton coupling to heme oxidation/reduction in the prototype maquette is a property neither of the cofactor itself nor of its axial ligands, but instead resides in the supporting protein matrix.

(D) Protein Side Chains. Only glutamate and lysine side chains remain as viable, simple candidates for releasing or accepting protons depending upon the heme oxidation state in heme-$(\alpha ss\alpha)_2$. Both amino acids, because of their highly polar character, were originally designed into the prototype $(\alpha ss\alpha)_2$ to provide an array of complementary charges at exterior positions of the bundle. Glutamate side chains with a pK value of 4.4 when free in solution are suitable candidates for the source of redox-linked proton binding/release in the prototype maquette in the low-pH region. However, to account for the E_m/pH relationship of the prototype maquette, the pK values of glutamate residues should be shifted to higher values as has been seen in some natural proteins (*46*−*48*). In the high-pH region, lysine residues with a solution pK value of 10.0 are feasible candidates with similar considerations. The pH-dependent behavior of the glutamates is more easily monitored via spectroscopic methods, and consequently these residues were the focus of our studies.

Figure 1B illustrates that 28 glutamates in the $(\alpha ss\alpha)_2$ maquette occupy the heptad **b** and **c** positions. However, only a few are close to the heme binding site. The most promising candidate for proton coupling to heme oxidation/reduction is Glu 11, which follows the heme-ligating histidine at position 10. Computer modeling suggests that Glu 11 can be brought to within 3−4 Å of the heme iron. Glu 12 at the heptad **c** position is also close in sequence to His 10, but modeling suggests that this residue is oriented in a direction away from the heme. Glu 18, at the heptad **b** position, although two helical turns below Glu 11 and hence further away from the heme, could also possibly contribute to redox-linked proton binding/release.

Unprotonated and protonated carboxylates can be distinguished by their characteristic infrared signatures (*49*) which permits direct pK determination of glutamate side chains in

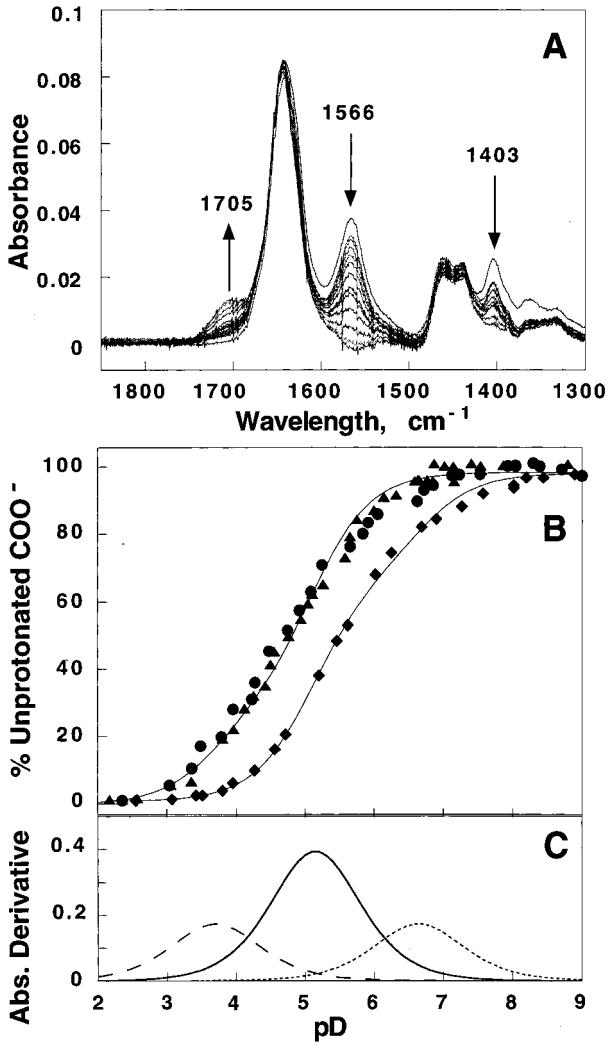

FIGURE 7: (A) FTIR pH titration of the apo-$(\alpha ss\alpha)_2$ in D_2O in the presence of 100 mM NaCl. Spectra shown correspond to pD values of 9.0, 7.53, 6.82, 5.91, 5.65, 5.24, 5.07, 4.74, 4.47, 4.22, 3.48, 3.03, and 2.35. The arrows indicate titrations of resonances sensitive to carboxylate protonation with varying pD. (B) Protonation of glutamates monitored by the amplitude of the 1566 cm^{-1} peak in the apo-$(\alpha ss\alpha)_2$ (●), oxidized heme-$(\alpha ss\alpha)_2$ (▲), and reduced heme-$(\alpha ss\alpha)_2$ (◆) maquettes. The lines represent a fit according to a simple model in which the majority of the glutamates retain the same p*K* value in the oxidized and the reduced states of the protein, but a minor population of glutamates shift their p*K* from low in the oxidized state to high in the reduced state. (C) The relative number of protons released in an alkaline pH titration by the population of glutamates with fixed p*K* value (solid line, 70%, p*K* 5.1) and the population of glutamates with redox-sensitive p*K* (dashed line, oxidized state, p*K* 3.7; dotted line, reduced state, p*K* 6.7).

the prototype maquette. Figure 7A shows the amide I and II regions of the infrared spectrum of the prototype apo-$(\alpha ss\alpha)_2$ obtained in D_2O. Three distinct peaks are observed in the spectrum that reflect the protonation state of carboxylates. These include the asymmetric and symmetric COO^- stretches at 1566 and 1403 cm^{-1}, respectively, that are visible at high pD, and which are transformed into the C═O stretch of the COOD group at 1705 cm^{-1} at low pD. The acid/base titration of the 1566 cm^{-1} band is shown in Figure 7B. Although the abundance of glutamates in the prototype maquette makes the assignment of individual protonation events difficult, measurement of the distributed p*K* values of the ensemble of glutamates in the protein is readily observed. To satisfactory describe pD titration data of the apo-bundle, at least two p*K* values are required on either side of the isolated solution glutamate p*K* value. The titration curve of the oxidized heme-$(\alpha ss\alpha)_2$ is similar to the apo-$(\alpha ss\alpha)_2$ within experimental error. However, in the reduced state, when compared to the oxidized heme-$(\alpha ss\alpha)_2$ or apo-$(\alpha ss\alpha)_2$, there is a noticeable loss of population with low p*K* values and a corresponding appearance of a population with high p*K* values. The data sets for the reduced and the oxidized maquettes were simultaneously modeled by assuming the presence of a major population of glutamates with the same p*K* value in both the oxidized and the reduced states and a population of glutamates which raise their p*K* values considerably upon heme reduction. The fitting procedure (Figure 7C) reveals a 70% population of glutamates (about 20) in the heme-$(\alpha ss\alpha)_2$ maquette in both the oxidized and the reduced state protonating at a p*K* of 5.1, while the other 30% of glutamates (about 8) shift their p*K* values from 3.7 in the oxidized state to 6.7 in the reduced state. Although the glutamate p*K* shifts are likely more complex than described here, the quality of the fit obtained with the simple model suggests that a more complex treatment is unwarranted at this stage. The presence of high p*K* glutamates only in the reduced heme-$(\alpha ss\alpha)_2$ is in concert with the pK_{red} at 7.0 obtained independently from the redox titration data. This finding satisfies the major criteria for the glutamate side chains being the source of the redox-linked proton exchange in the low pH range.

Site-Selected Glutamine for Glutamate Side Chain Variants of the Prototype Maquette. To further pursue the possibility that the glutamate residues participate in the redox-linked proton exchange, several variants of the prototype maquette were constructed with non-proton-exchanging glutamines (Gln, Q) substituted for candidate glutamates (Glu, E). Replacement of glutamates with their amide derivatives was not expected to disrupt the packing of the bundle interior because of their similar size, polarity, and α-helix-promoting character (*50*). Three different variants of the prototype maquette were designed and synthesized. In the first variant, $(\alpha ss\alpha)_2$-E11Q, only the glutamate closest to the heme, at position 11 in each helix, was replaced by glutamine. In the second variant, $(\alpha ss\alpha)_2$-E11,18,25Q, three glutamates, all at the heptad **b** positions, were substituted by glutamines. In the third variant, $(\alpha ss\alpha)_2$-EallQ, the entire glutamate population was removed and replaced by glutamines.

Despite the rather significant changes in the protein sequence, all three variants remained water soluble, fully helical and stable at neutral and low pH, and bound heme with high affinity (see Table 1). Equilibrium ultracentrifugation together with size-exclusion chromatography demonstrated that two of the variants, $(\alpha ss\alpha)_2$-E11Q and $(\alpha ss\alpha)_2$-E11,18,25Q, retain the aggregation state of a four-helix bundle. The $(\alpha ss\alpha)_2$-EallQ maquette eluted at much longer times than the other two variants and was proven to bind to the column (S. Huang, unpublished observations). Consequently, only equilibrium ultracentrifugation data were used to determine its molecular mass. The observed molecular mass of the heme-$(\alpha ss\alpha)_2$-EallQ maquette at pH 8.5 was higher than those of other variants. However, a similar experiment with the apo form of the peptide yielded a molecular mass of 15.7 kDa, very close to 15.5 kDa, the expected molecular mass of a four-helix bundle. The

Table 1: Comparison of Physical Properties of Heme-$(\alpha ss\alpha)_2$, Heme-$(\alpha ss\alpha)_2$-E11Q, Heme-$(\alpha ss\alpha)_2$-E11,18,25Q, and Heme-$(\alpha ss\alpha)_2$-EallQ Maquettes at Neutral and Low pH Values

	molecular mass (kDa)									
		equilibrium ultracentr		size exclusion			E_m (mV)		$\Delta G°$ [a] (kcal/mol)	
protein	expected	pH 8.5	pH 4.0	pH 8.5	pH 4.0	1st heme K_d (nM)	pH 8.5	pH 4.0	pH 8.5	pH 4.0
heme−$(\alpha ss\alpha)_2$	15.538	15.7	18.8	20.1	19.9	12	−156	+5	14.5	19.4
heme−$(\alpha ss\alpha)_2$ E11Q	15.538	15.5	19.5	20.1	16.2	8	−104	−19	14.8	18.6
heme−$(\alpha ss\alpha)_2$ E11,18,25Q	15.538	15.5	18.9	16.7	18.3	0.2	−98	−53	14.3	14.9
heme−$(\alpha ss\alpha)_2$ EallQ	15.538	24.0[b]	18.5	−[c]	−[c]	0.4	−92	−53	14.8	14.4

[a] $\Delta G°$ values were calculated from chemical denaturation experiments using eq 1. [b] Equilibrium ultracentrifugation of this peptide in the apo form yielded a molecular mass of 15.7 kDa. [c] This peptide did not elute well on the column; hence, only equilibrium centrifugation data were used to determine peptide molecular mass.

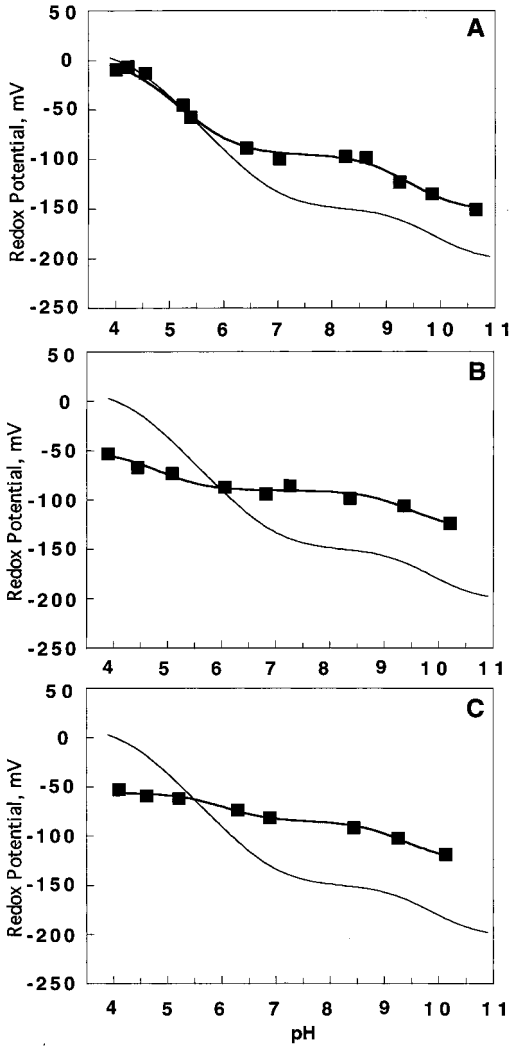

FIGURE 8: pH dependency of the redox midpoint potential of the Glu to Gln variants: (A) heme-$(\alpha ss\alpha)_2$-E11Q, (B) heme-$(\alpha ss\alpha)_2$-E11,18,25Q, (C) heme-$(\alpha ss\alpha)_2$-EallQ. The data were fit to eq 3 with two acid/base groups involved. For comparison, the curve used to fit the redox potential data of the prototype heme-$(\alpha ss\alpha)_2$ is also shown. Buffers and conditions are as described in Figure 3A.

observed molecular mass of heme-$(\alpha ss\alpha)_2$-EallQ at pH 4 was also very close to those of other variants. Thus, we consider the $(\alpha ss\alpha)_2$-EallQ maquette to assemble into four-helix bundles just like the other two variants, although some fraction of this maquette might assume higher aggregation states of six- or eight-helix bundles.

Figure 8 describes the E_m/pH relationships of the glutamine variants in comparison to the prototype maquette. Figure 8A shows that the E_m of heme-$(\alpha ss\alpha)_2$-E11Q assumes a less prominent pH dependency between pH 4 and 7. When compared to the prototype maquette, the pK^1_{ox} of the heme-$(\alpha ss\alpha)_2$-E11Q appears unchanged, while pK^1_{red} is lowered by almost 1 pH unit from 7.0 to 6.1. These results are consistent with the idea that Glu 11 is buried inside the bundle, and when the heme is in the ferrous state, its pK value is substantially higher than the average value for the other glutamates in the bundle. Figure 8B shows that further substitution of glutamates for glutamines in heme-$(\alpha ss\alpha)_2$-E11,18,25Q leads to an almost complete loss of the E_m dependence on pH in the region between pH 4 and 7. Figure 8C shows that removal of the remaining glutamates at the heptad **c** positions in heme-$(\alpha ss\alpha)_2$-EallQ produces no further significant changes. The E_m/pH relationships of the glutamate/glutamine variants prove the significant involvement of Glu 11 in the proton coupling to the heme oxidation/reduction. However, it is clear that in the absence of Glu 11, proton coupling, although decreased in magnitude, still proceeds via an alternative route. In particular, Glu 18 (and possibly Glu 12 and Glu 25) acts in response to the change in the heme oxidation state. The remaining relatively small change in the redox potential (about 30 mV per 4.5 pH units) of the heme-$(\alpha ss\alpha)_2$-E11,18,25Q and heme-$(\alpha ss\alpha)_2$-EallQ variants in the low-pH region could be due to protonation of heme propionic acids as suggested by the RR studies on the prototype maquette discussed above.

Despite the pronounced differences in the E_m/pH profiles of the heme-$(\alpha ss\alpha)_2$ variants at low pH, all the variants behave alike above pH 7. All four maquettes retain the characteristic trend to pH independence between pH 7 and 9 and pH dependence above pH 9 with similar alkaline pK values in both heme oxidation states. These results suggest that at higher pH values, redox-linked proton coupling is due to an independent source and proceeds through the same mechanism for all variants. It seems most likely that the candidates to perform proton coupling in the high-pH region will be found among lysine side chains that operate in a fashion analogous to that of glutamates in the lower pH region.

DISCUSSION

Designing Noncovalent Binding of Heme Centers in Maquettes. The tight (nanomolar) heme binding affinity shown in the prototype maquette serves as evidence that the hydrophobic heme pocket of natural heme proteins is suitably mimicked by the extensive leucine core supplemented by aromatic residues in the heme protein maquettes. The

internal placement of the ligating histidines at heptad **a** positions directed toward the hydrophobic interior has recently been shown to be a crucial component of the design (B. R. Gibney and P. L. Dutton, unpublished results). In the work presented here, replacement of charged glutamates with glutamines at neutral pH further increases the overall hydrophobicity of the bundle, resulting in increased heme binding affinity (Table 1). The K_d values of the heme for $(\alpha ss\alpha)_2$-E11,18,25Q and $(\alpha ss\alpha)_2$-EallQ maquettes are in the subnanomolar range, the highest affinity so far achieved in synthetic heme proteins.

Lowering the pH below 4 causes protonation of heme-ligating histidines which results in heme dissociation from the bundle (Figure 3). The lower pH does not displace the ferric heme as easily as the ferrous heme, perhaps because the more positively charged iron electrostatically discourages histidine protonation. Figure 3 also shows that at very high pH the differential pH dependency of the ferrous and ferric heme affinity is reversed. Here the ferric heme more readily dissociates, probably because the negatively charged hydroxyls are preferentially attracted to the positively charged ferric heme iron.

Surprisingly, making the heme itself more hydrophobic by esterifying the propionic acids decreases the apparent heme binding affinity by approximately 1000-fold. Whereas DME-heme has been shown to bind tightly to the hydrophobic pocket of myoglobin (*51*), our relatively small bundles might prohibit complete burial of the esterified cofactor and hence inhibit its binding. The amphipathic character of the natural propionate-containing heme may allow a more favorable orientation in the synthetic bundle with the porphyrin ring embedded in the hydrophobic core and the propionic acids pointing outward into aqueous solution (*38*).

These observations on heme binding can be summarized in a principle of design for construction of redox/proton-coupled proteins, that has obvious connections to previous work in natural proteins. *High-affinity heme binding sites can be designed by providing the heme with a highly hydrophobic environment and by optimizing the interactions with its axial ligands through adjusting ligand orientation, pH, and redox conditions.*

Maquette Stability at Extremes of pH. The limited pH range for stability of many natural proteins often prevents the simultaneous measurement of the oxidized and the reduced p*K* values in proton-coupled redox reactions and complicates the task of assigning the acid/base group(s) involved. Our heme protein maquettes were designed with an extraordinary folding stability. This stability extends to extreme pH conditions, allowing us to perform redox titration experiments over a wide pH range and to obtain p*K* values in both redox states. Nevertheless, we expect the stability of the bundle to alter with a change in protonation state of 28 glutamates and/or 24 lysines. Many coiled-coil proteins, both natural and synthetic, have been reported to be more resistant to denaturation at acidic pH in the presence of high salt concentration (*52*−*58*). This was explored in synthetic two-helix bundles with glutamates and lysines on the helical interface positions (*57*) where the loss of favorable electrostatic interaction upon glutamate protonation was outweighed by the increase in bundle hydrophobicity. Similar behavior is encountered in our four-helix bundle heme protein maquettes. Lowering the pH from neutral to acidic values results in a substantial increase in stability of the heme-$(\alpha ss\alpha)_2$ maquette and heme-$(\alpha ss\alpha)_2$-E11Q (Table 1). In contrast, the stability of the peptides with higher glutamine content [heme-$(\alpha ss\alpha)_2$-E11,18,25Q and heme-$(\alpha ss\alpha)_2$-EallQ] does not show any significant changes with pH, as expected (Table 1). The increase in stability of the glutamate-containing peptides at low pH can be explained by the increase in hydrophobicity of the bundle core when certain glutamate side chains are protonated; this option is not possible for heme-$(\alpha ss\alpha)_2$-EallQ. This illustrates a second principle of redox/proton coupling design: *to explore proton/electron coupling, proteins should be designed with extraordinary stability to avoid unfolding associated with side chain protonation changes at pH extremes.*

Maquette Side Chain pK Distribution. The p*K* values of side chains in natural proteins are frequently found to be shifted from their isolated aqueous solution values. Such alterations in p*K* values have been attributed to charge−charge interactions within the protein and have been reproduced quite well in theoretical studies (*59*−*61*). Despite their structural simplicity, heme protein maquettes also exhibit distributed p*K* values in the protonation of glutamate side chains. Nearby positive lysines would tend to lower glutamate p*K* values, while nearby negative glutamates would raise their p*K* values. However, most electrostatic interactions at the exterior positions of the bundle are expected to be screened by the high ionic strength (100 mM NaCl) maintained throughout the investigation. The clear presence of several glutamates with p*K* values higher than the solution p*K* value even in the apo-$(\alpha ss\alpha)_2$ and ferric heme-$(\alpha ss\alpha)_2$ provides additional support that certain glutamates are at least partially buried inside the bundle. However, the population of the high-p*K* glutamates in the prototype ferrous heme-$(\alpha ss\alpha)_2$ is conspicuous. The FTIR analysis demonstrates that several glutamates, most likely occupying the heptad **b** position, are in the hydrophobic interior of the ferrous heme-$(\alpha ss\alpha)_2$, perhaps being drawn in as a part of the repacking of the structure upon incorporation of the heme macrocycle. When the heme is oxidized, a conformational change could move these interior glutamates outside the bundle, where their p*K* would fall back to near the solution p*K* value of 4.4. Alternatively, and we believe more likely, the interior glutamates could stay buried upon heme oxidation, but deprotonate, thus providing stabilization for the positive charge on the ferric heme iron. In this case, the p*K* of the glutamates interacting with the charge on the ferric heme could be lowered even further below the solution p*K* value. The analysis of the FTIR data supports the second scenario, in which a population of glutamates in the prototype maquette shift their p*K* value from 6.7 to 3.7 upon heme oxidation. These observations manifest a third principle of redox/proton coupling design: *hydrophobic burial of protonatable residues around the heme cofactor provides the means to shift the acidic side chain pK values up into the neutral range and to shift them down in response to heme oxidation, thereby enabling redox-linked proton coupling in the physiological pH range.*

Controlling Heme Redox Potential through Charge Compensation. The redox potential of the prototype maquette in the neutral pH range, above pK^1_{red}, is −156 mV. This value is strongly influenced by the Glu 11 carboxylate anion which stabilizes the positively charged ferric heme relative

to the neutral ferrous heme and hence lowers the heme redox potential. Replacement of anionic glutamate for neutral glutamine is expected to raise the heme redox potential by the amount inversely proportional to the dielectric distance between the glutamate side chain and the heme iron. This is clearly demonstrated in glutamine variants of the prototype maquette: elimination of the glutamate closest to the heme in heme-$(\alpha ss\alpha)_2$-E11Q results in a 50 mV increase in the redox potential; removing additional glutamates further away from the heme in heme-$(\alpha ss\alpha)_2$-E11,18,25Q and heme-$(\alpha ss\alpha)_2$-EallQ produces only an additional 5 and 10 mV rise, respectively. The 50−60 mV increase in E_m due to the glutamate to glutamine substitution achieved in four-helix bundle heme protein maquettes is readily comparable to the 108 mV increase due to analogous aspartate to asparagine substitution in the highly hydrophobic heme pocket of myoglobin (*34*).

While replacement of a carboxylate for an amide group in the heme vicinity eliminates electrostatic stabilization of the ferric heme, it does not abolish the dipolar charge compensation due to the quite polar character of the amide group. This effect is demonstrated in myoglobin (*34*), where the wild-type protein with a nonpolar Val 68 exhibits a midpoint potential 80 mV higher than a mutant with an asparagine at this position. Likewise, in our synthetic bundles at pH values below pK^1_{ox}, where protonated glutamates are less polar than glutamines, the E_m of the glutamate containing prototype heme-$(\alpha ss\alpha)_2$ is 24 mV higher than that of heme-$(\alpha ss\alpha)_2$-E11Q and 58 mV higher than that of the multi-glutamine variants. We expect that substitution of a nonpolar residue (Val or Leu) at position 11 of the prototype maquette will raise the heme redox potential to yet higher values, offering the possibility to reproduce higher potentials observed in natural cytochromes.

Removal of the propionic acids from the heme group, as shown by studies of DME-heme-$(\alpha ss\alpha)_2$, results in about a 60 mV increase in the redox potential over the whole pH range. In addition, the pK values in both the oxidized and the reduced states are essentially the same as for the prototype heme-$(\alpha ss\alpha)_2$. The fact that the redox potential of the DME-heme-$(\alpha ss\alpha)_2$ is higher than that of heme-$(\alpha ss\alpha)_2$ at pH 4, where the heme propionic acids are protonated, could be explained by a structural difference between the binding of DME-heme and heme to the $(\alpha ss\alpha)_2$ maquette, with DME-heme being in a more hydrophobic environment. Alternatively, the DME-heme raised redox potential could be due to a decrease in water accessibility of the heme iron resulting from the increased hydrophobic interactions between the protein and the heme propionates.

Collectively, the above-noted observations exemplify a fourth principle of redox/proton coupling design: *elevation of heme redox potential can be achieved through elimination of charge-compensating protonatable residues. However, the magnitude of the increase in redox potential can be lessened if the elimination replaces the charged residue with a more polar one.*

Hierarchical Charge Compensation. We have shown that Glu 11 is the key source of proton coupling in the prototype maquette. As shown in Figure 1B, there are 4 glutamates occupying the 11 positions in each helix of the tetrahelix bundle. However, steric considerations dictate that only one of the glutamates at position 11, situated on helix A of the heme-occupied $\alpha ss\alpha$ subunit, will be oriented toward the heme, while the other one on helix B will be forced out into solution. The glutamates in an adjacent di-α-helical subunit are probably too far from the heme for strong coupling. Similar considerations show that one out of four glutamates at position 12, located on the helix B, could possibly interact with the heme, but would not be as close as Glu 11 and hence, in the presence of Glu 11, would not be expected to be a primary source of proton exchange.

Elimination of the proton binding/release site does not necessarily create a protein without redox/proton coupling. The profound electrostatic potential changes due to heme oxidation/reduction will recruit other available charged residues for heme charge compensation. Thus, removal of Glu 11 in the heme-$(\alpha ss\alpha)_2$-E11Q apparently leads to the promotion of another glutamate (Glu 12 or Glu 18) from a secondary to a primary role in the redox-dependent proton binding/release reaction in the prototype maquette, albeit with a decrease in the strength of the proton coupling. These findings are generally consistent with Coulomb's law which requires that the magnitude of the heme−glutamate interactions be inversely proportional to the dielectric distance between the glutamate carboxylates and the iron of the heme cofactor.

Together, the above-noted observations illustrate a fifth principle of redox/proton coupling design: *proton coupling to heme oxidation/reduction is generally distributed over many protonatable groups. Accordingly, engineering proteins with pH-independent redox behavior may require elimination of all acid/base residues within a large dielectric distance from the cofactor.*

Final Comments. The findings of the present study show that simple functionalization of minimal protein designs (*36*) offers a viable way to approach mechanistic questions of more complex natural proteins. Our success in reproducing proton-coupled redox reactions in a family of simple heme protein maquettes clearly shows that the effect is remarkably easy to achieve and that pK shifts could prove to be merely incidental when the heme redox potential does not play a crucial role in protein function. On the other hand, proton coupling to heme oxidation/reduction can clearly alter the E_m of the heme cofactor by a significant amount and hence is a means of establishing redox potential in vivo. The mechanism of redox-coupled proton exchange through a glutamate (or lysine) side chain described in this work has many of the basic characteristics required for the function of a proton pump, where a very strict conformational change in the protein is also coupled to oxidation/reduction and vectorial proton translocation.

The clear identification of glutamates as the source of redox-linked proton exchange in heme protein maquettes suggests that Glu and Asp residues should be searched for near heme sites of complex natural proteins exhibiting proton-coupled redox reactions. Literature suggestions that these residues play exactly such a role include the cytochrome bc_1 complex, where Glu and Asp residues have been tentatively identified as the source of the pH dependence of the redox potentials of the *b*-type hemes (*62*). In particular, examination of the recently available structure (*63*) points to a glutamate that is within 10 Å of the iron in heme b_L and an aspartate residue within 12 Å of the b_H heme. The reduction of ubiquinone in the Q_B site of the photosynthetic

reaction centers from *Rhodobacter spheroides* is also accompanied by proton uptake, assigned to Glu L212 near Q_B (*64*, *65*) on the basis of redox-induced FTIR spectral changes. Finally, recent work using the same technique by Hellwig et al. (*66*) on cytochrome *c* oxidase identifies the involvement of Glu 278 as the source of proton coupling to oxidation/reduction of heme *a*, which might be involved in the pathway of proton translocation across the membrane.

ACKNOWLEDGMENT

We are grateful to James Lear and Wei Lau for providing assistance with ultracentrifugation experiments. We thank Jane Vanderkooi and Wayne Wright for useful ideas and help with the FTIR experiments. We also thank Edward A. Berry for providing us with coordinates of the bc_1 complex before they were deposited to the Brookhaven Protein Databank. We acknowledge the Protein Chemistry Laboratory of the University of Pennsylvania for performing mass spectroscopic analyses of all peptides used in this study.

REFERENCES

1. Lancaster, C. R., Michel, H., Honig, B., and Gunner, M. R. (1996) *Biophys. J. 70*, 2469−2492.
2. Rabenstein, B., Ullmann, G. M., and Knapp, E. W. (1998) *Biochemistry 37*, 2488−2495.
3. Bashford, D., Karplus, M., and Canters, G. W. (1988) *J. Mol. Biol. 203*, 507−510.
4. Chance, B., Crofts, A. R., Nishimura, M., and Price, B. (1970) *Eur. J. Biochem. 13*, 364−374.
5. Papa, S., Guerrieri, F., and Izzo, G. (1979) *FEBS Lett. 105*, 213−216.
6. Xavier, A. V. (1985) *Frontiers in Bioinorganic Chemistry*, VCH, Weinheim, Germany.
7. Clark, W. M. (1960) *Oxidation−Reduction Potentials of Organic Systems*, Williams and Wilkins, Baltimore.
8. Dutton, P. L. (1978) *Methods Enzymol. 54*, 411−435.
9. Petty, K., Jackson, J. B., and Dutton, P. L. (1979) *Biochim. Biophys. Acta 546*, 17−42.
10. Keske, J. M. (1992) *Experimental and Theoretical Approaches to Quinone Binding and Function at the Q_A Site of Photosynthetic Reaction Centers*, University of Pennsylvania, Ph.D. Dissertation, Philadelphia, PA.
11. Swallow, A. J. (1982) in *Function of Quinones in Energy Conserving Systems* (Trumpower, B. L., Ed.) pp 59−72, Academic Press, Inc., New York.
12. DeVault, D. (1976) *J. Theor. Biol. 62*, 115−139.
13. Ohnishi, T. (1976) *Eur. J. Biochem. 64*, 91−103.
14. Meinhardt, S. W., Kula, T., Yagi, T., Lillich, T., and Ohnishi, T. (1987) *J. Biol. Chem. 262*, 9147−9153.
15. Dutton, P. L., Moser, C. C., Sled, V. D., Daldal, F., and Ohnishi, T. (1998) *Biochim. Biophys. Acta 1364*, 245−260.
16. Petty, K. M., and Dutton, P. L. (1976) *Arch. Biochem. Biophys. 172*, 346−353.
17. Rich, P. R., Jeal, A. E., Madgwick, S. A., and Moody, A. J. (1990) *Biochim. Biophys. Acta 1018*, 29−40.
18. Wilson, D. F., Lindsay, J. G., and Brocklehurst, E. S. (1972) *Biochim. Biophys. Acta 256*, 277−286.
19. Blair, D. F., Ellis, W. R., Jr., Wang, H., Gray, H. B., and Chan, S. I. (1986) *J. Biol. Chem. 261*, 11524−11537.
20. Pettigrew, G. W., Bartsch, R. G., Meyer, T. E., and Kamen, M. D. (1978) *Biochim. Biophys. Acta 503*, 509−523.
21. Leitch, F. A., Moore, G. R., and Pettigrew, G. W. (1984) *Biochemistry 23*, 1831−1838.
22. Moore, G. R., Pettigrew, G. W., Pitt, R. C., and Williams, R. J. (1980) *Biochim. Biophys. Acta 590*, 261−271.
23. Saraiva, L. M., Thomson, A. J., Le Brun, N. E., Liu, M. Y., and Payne, W. J. *Biochem. Biophys. Res. Commun. 204*, 120−128.
24. Moore, G. R., Harris, D. E., Leitch, F. A., and Pettigrew, G. W. (1984) *Biochim. Biophys. Acta 764*, 331−342.
25. Costa, H. S., Santos, H., Turner, D. L., and Xavier, A. V. (1992) *Eur. J. Biochem. 208*, 427−433.
26. Barker, P. D., Nerou, E. P., Cheesman, M. R., Thomson, A. J., de Oliveira, P., and Hill, H. A. (1996) *Biochemistry 35*, 13618−13626.
27. Barker, P. D., and Freund, S. M. (1996) *Biochemistry 35*, 13627−13635.
28. La Mar, G. N., Jackson, T. J., and Bartsch, R. G. (1981) *J. Am. Chem. Soc. 103*, 4405−4410.
29. Saraiva, L. M., Liu, M. Y., Payne, W. J., Legall, J., Moura, J. J., and Moura, I. (1990) *Eur. J. Biochem. 189*, 333−341.
30. Moura, I., Liu, M. Y., Costa, C., Liu, M. C., Pai, G., Xavier, A. V., LeGall, J., Payne, W. J., and Moura, J. J. (1988) *Eur. J. Biochem. 177*, 673−682.
31. Moore, G. R., Williams, R. J., Peterson, J., Thomson, A. J., and Mathews, F. S. (1985) *Biochim. Biophys. Acta 829*, 83−96.
32. Saraiva, L. M., Denariaz, G., Liu, M. Y., Payne, W. J., Le Gall, J., and Moura, I. (1992) *Eur. J. Biochem. 204*, 1131−1139.
33. Cutler, R. L., Davies, A. M., Creighton, S., Warshel, A., Moore, G. R., Smith, M., and Mauk, A. G. (1989) *Biochemistry 28*, 3188−3197.
34. Varadarajan, R., Zewert, T. E., Gray, H. B., and Boxer, S. G. (1989) *Science 243*, 69−72.
35. Varadarajan, R., Lambright, D. G., and Boxer, S. G. (1989) *Biochemistry 28*, 3771−3781.
36. DeGrado, W. F., Wasserman, Z. R., and Lear, J. D. (1989) *Science 243*, 622−628.
37. Robertson, D. E., Farid, R. S., Moser, C. C., Urbauer, J. L., Mulholland, S. E., Pidikiti, R., Lear, J. D., Wand, A. J., DeGrado, W. F., and Dutton, P. L. (1994) *Nature 368*, 425−432.
38. Kalsbeck, W. A., Robertson, D. E., Pandey, R. K., Smith, K. M., Dutton, P. L., and Bocian, D. F. (1996) *Biochemistry 35*, 3429−3438.
39. Hodges, R. S. (1996) *Biochem. Cell. Biol. 74*, 133−154.
40. Betz, S. F., Bryson, J. W., and DeGrado, W. F. (1995) *Curr. Opin. Struct. Biol. 5*, 457−463.
41. Kharakoz, D. P. (1997) *Biochemistry 36*, 10276−10285.
42. Mok, Y. K., de Prat Gay, G., Butler, P. J., and Bycroft, M. (1996) *Protein Sci. 5*, 310−319.
43. Desbois, A., and Lutz, M. (1992) *Eur. Biophys. J. 20*, 321−335.
44. Othman, S., Le Lirzin, A., and Desbois, A. (1994) *Biochemistry 33*, 15437−15448.
45. Hu, S., Smith, K. M., and Spiro, T. G. (1996) *J. Am. Chem. Soc. 118*, 12638−12646.
46. Kuramitsu, S., Hamaguchi, K., Miwa, S., and Nakashima, K. (1980) *J. Biochem. 87*, 771−778.
47. Davoodi, J., Wakarchuk, W. W., Campbell, R. L., Carey, P. R., and Surewicz, W. K. (1995) *Eur. J. Biochem. 232(3)*, 839−843.
48. Brown, L. S., Kamikubo, H., Zimanyi, L., Kataoka, M., Tokunaga, F., Verdegem, P., Lugtenburg, J., and Lanyi, J. K. (1997) *Proc. Natl. Acad. Sci. U.S.A. 94*, 5040−5044.
49. Goormaghtigh, E., Cabiaux, V., and Ruysschaert, J.-M. (1994) *Subcell. Biochem. 23*, 329−362.
50. Schultz, G. E., and Schirmer, R. H. (1979) *Principles of Protein Structure*, Springer-Verlag, New York.
51. Hargrove, M. S., Wilkinson, A. J., and Olson, J. S. (1996) *Biochemistry 35*, 11300−11309.
52. Lowey, S. (1965) *J. Biol. Chem. 240*, 2421−2427.
53. Lau, S. Y., Taneja, A. K., and Hodges, R. S. (1984) *J. Biol. Chem. 259*, 13253−13261.
54. Hodges, R. S., Semchuk, P. D., Taneja, A. K., Kay, C. M., Parker, J. M., and Mant, C. T. (1988) *Pept. Res. 1*, 19−30.
55. Hodges, R. S., Zhu, B. Y., Zhou, N. E., and Mant, C. T. (1994) *J. Chromatogr. A 676*, 3−15.
56. O'Shea, E. K., Klemm, J. D., Kim, P. S., and Alber, T. (1991) *Science 254*, 539−544.

57. Zhou, N. E., Kay, C. M., and Hodges, R. S. (1994) *Protein Eng. 7*, 1365−1372.
58. Yu, Y., Monera, O. D., Hodges, R. S., and Privalov, P. L. (1996) *J. Biophys. Chem. 59*, 299−314.
59. Sampogna, R. V., and Honig, B. (1996) *Biophys. J. 71(3)*, 1165−1171.
60. Alexov, E. G., and Gunner, M. R. (1997) *Biophys. J. 74(5)*, 2075−2093.
61. Russell, S. T., and Warshel, A. (1985) *J. Mol. Biol. 185*, 389−404.
62. Baymann, F., Robertson, D. E., and Mantele, W. (1995) in *Photosynthesis: from Light to Biosphere* (Mathis, P., Ed.) pp 611−614, Kluwer Academic Publishers, Dordrecht.
63. Zhang, Z., Huang, L., Shulmeister, V. M., Chi, Y. I., Kim, K. K., Hung, L. W., Crofts, A. R., Berry, E. A., and Kim, S. H. (1998) *Nature 392*, 677−684.
64. Hienerwadel, R., Grzybek, S., Fogel, C., Kreutz, W., Okamura, M. Y., Paddock, M. L., Breton, J., Nabedryk, E., and Mantele, W. (1995) *Biochemistry 34*, 2832−2843.
65. Nabedryk, E., Breton, J., Hienerwadel, R., Fogel, C., Mantele, W., Paddock, M. L., and Okamura, M. Y. (1995) *Biochemistry 34*, 14722−14732.
66. Hellwig, P., Rost, B., Kaiser, U., Ostermeier, C., Michel, H., and Mantele, W. (1996) *FEBS Lett. 385*, 53−57.

BI9816857